Progress In Electromagnetics Research B, Vol. 70, 101–112, 2016

Investigation of Alignment Errors on Multi-Static Microwave Imaging Based on Frequency-Diverse Metamaterial Apertures

Hayrettin Odabasi*, Mohammadreza F. Imani, Guy Lipworth, Jonah Gollub, and David R. Smith

Abstract—We examine the effect of alignment errors on the performance of a frequency-diverse imaging system composed of metamaterial apertures. In a frequency-diverse imaging system, a sequence of distinct radiation patterns, indexed by frequency, provides measurements of the spatial content of a scene. This set of measurements can then be used to obtain a high-fidelity estimate of the scene using computational imaging techniques. As with any computational imaging system, realizing the full potential of the frequency-diverse system requires accurate characterization of the complex radiation patterns. This characterization entails precise knowledge of the locations and orientations of the transmitters and receivers; any discrepancy between the modeled and actual locations will introduce phase error and degrade the quality of image reconstructions. Here, we study the effect of various misalignment errors on the performance of a sparse, bi-static, frequency diverse imaging system and provide an estimate on the levels of error within which the frequency-diverse apertures can reconstruct high quality images. Depending on the misalignment type (i.e., displacement, rotation) and direction the phase error can change significantly. As a result, for instance, we show that the imaging system is significantly less sensitive to cross-range displacement errors than to range displacement errors. We also show that the displacement errors are reduced for larger systems comprising many sub-apertures, due to the reduced averaged phase error. We find the impact of rotational errors is small compared to that of the displacement errors. However, as the sub-aperture size increases, rotational errors become more pronounced, becoming severe for larger sub-apertures with multiple feeds.

1. INTRODUCTION

Microwave waveforms can penetrate non-metallic objects and have no ionizing effect on the human body two advantages that make them well-suited for applications such as security screening and threat detection [1], biomedical diagnosis [2], and through-wall imaging [3]. Conventional imaging systems have relied on mechanical scanning or electronic beam-forming. These systems can achieve high quality images, yet are often bulky, expensive, or time consuming in practice. To circumvent these drawbacks, computational imaging systems have been developed that rely predominantly on post-processing to reconstruct images and can harness unconventional measurements and hardware [4–8]. For instance, a single pixel terahertz imaging system has been developed that can obtain high quality images using a single detector and a random set of masks [4]. Computational imaging schemes have also been utilized in computer generated holography [5], spatial light modulators [6], and multiple scattering mediums [7].

Recently, frequency-diverse metamaterial apertures have been demonstrated as a platform for computational imaging schemes at microwave frequencies [8–12]. The frequency-diverse aperture is of particular interest, since it in principle requires only a frequency sweep to generate a series of diverse waveforms that can be used to acquire spatial information. One version of a metamaterial imager consists of a parallel plate waveguide, in which the top plate is patterned with an array of metamaterial

Received 28 May 2016, Accepted 11 October 2016, Scheduled 27 October 2016
* Corresponding author: Hayrettin Odabasi (hayrettin.odabasi@duke.edu).
The authors are with the Department of Electrical and Computer Engineering, Duke University, Durham, NC 27708, USA.

resonators. Each resonator is a patterned iris cut into the upper conducting plate, that resonates at a frequency determined by its geometry. Although many metamaterial designs can be applied to form the elements, the complementary electric-field-coupled resonator (cELCs) represents a natural choice, since it behaves as a polarizable magnetic dipole with resonance frequency tuned by adjusting its geometry, and is easily integrated with waveguide geometries [13]. The cELC is excited by the magnetic field of the waveguide mode that propagates within the parallel plate waveguide, excited by one or more coaxial feeds introduced in the lower plate. The connector injects a cylindrical transverse electric-magnetic (TEM) mode that propagates away from the feeding point and couples to the metamaterial elements. At each driving frequency, a spatially diverse radiation pattern is generated, resulting from the coupling of the TEM waveguide mode to those cELCs whose resonance frequencies match the driving frequency. The radiative modes generated by the metamaterial aperture thus produce a set of distinct radiation patterns, or measurement modes, indexed by frequency. Applying computational imaging techniques to these measurement modes allows a scene to be reconstructed.

Computational imaging approaches are advantageous as they can make use of complex field patterns or measurement modes, reducing hardware constraints or enabling unconventional hardware paradigms; however, the flexibility associated with computational imaging systems comes at the cost of requiring a detailed characterization of the field patterns and a greater burden on the processing for reconstruction. As with other coherent imaging systems, the performance of the frequency-diverse imaging system depends critically on the accurate and detailed knowledge of the field patterns throughout the scene domain. These fields are used in conjunction with a forward model to construct a measurement matrix that relates the scene reflectivity to the measurements [9, 11]. Scene estimation then consists of inverting (or approximately inverting) this measurement matrix to determine the reflectivity values. The forward model also requires a scattering model for objects in the scene taken here as the first Born approximation which we assume is accurate for the purposes of this study.

The measurement matrix is calculated based on the field patterns generated assuming specific aperture locations and orientations [11]. When the aperture is ultimately used to image a scene, however, the expected aperture locations and orientations can be different from those of the aperture actually used, due to misalignments or other environmental influences that act over time. Improperly accounting for the alignment of the modeled aperture introduces phase error into the forward scattering model. Coherent measurements are particularly sensitive to phase errors, which can significantly deteriorate imaging performance. For example, the degradation of image quality as a result of phase errors in synthetic aperture radar (SAR) has been investigated in [14–19] and various methods have been proposed to detect and correct them [14–22]. Understanding the sources of similar errors, and the corresponding acceptable tolerances, is thus an important consideration for practical implementations of frequency-diverse apertures.

Here we investigate the effect of misalignment error defined as the displacement or rotation of transmitter or receiver apertures from their assumed locations and orientations on the imaging performance of a frequency diverse metamaterial imager. Misalignment of the transmitter and receiver apertures introduces predominantly a phase error into the system. Since frequency diverse metamaterial apertures are electrically large and have complex radiation patterns, they can be particularly prone to these types of errors. Furthermore, these apertures are often experimentally characterized, and characterization error can contribute further to phase errors. In practice, some misalignment is inevitable, either during the experimental characterization, or as a result of misplacement or rotation during installation of apertures in the aggregate system. The misalignment becomes a particular challenge for millimeter wave imaging, as the required size of the system becomes extremely large compared with the wavelengths corresponding to the operating frequencies. Here, we present a thorough investigation of the impact of misalignment error for various system parameters, such as the number of apertures and the size of the apertures.

In our studies, we focus on a specific architecture proposed for a frequency-diverse metamaterial aperture in [8], and later used as the basis for several variants [9–12]. We consider this architecture as it is relatively easy to model and because samples have been fabricated and implemented successfully in imaging experiments. We expect, however, the results obtained to be generally applicable to many other types of frequency-diverse apertures, such as the mode-mixing cavities recently pursued in [23] or the dynamic metamaterial apertures demonstrated in [24].

2. DESCRIPTION OF THE SYSTEM

A schematic depiction of the sparse, multi-static frequency-diverse metamaterial imaging system considered in this paper is illustrated in Fig. 1. In Fig. 1(a), metamaterial apertures (or panels) are used as transmitting antennas while open ended waveguide (OEWG) probes are used as receiving antennas. In Fig. 1(b), metamaterial panels are used both for transmitting and receiving antennas. In a typical implementation, a single radio is used to drive the system, with the signal sequentially coupled to the various transmitting apertures (as well as the OEWGs) via mechanical or electrical switches. It is of practical interest to study and compare both the panel-to-probe and panel-to-panel cases. Thus the configuration in Figs. 1(a), (b) is designed to be able to switch between metamaterial apertures and OEWGs, without altering the positions of the apertures. Each of these cases offers its own advantages: OEWGs have large bandwidth and low-gain, ensuring that an ample signal is collected from all possible directions and at all frequencies; while metamaterial panels can provide a more diverse set of measurements [25].

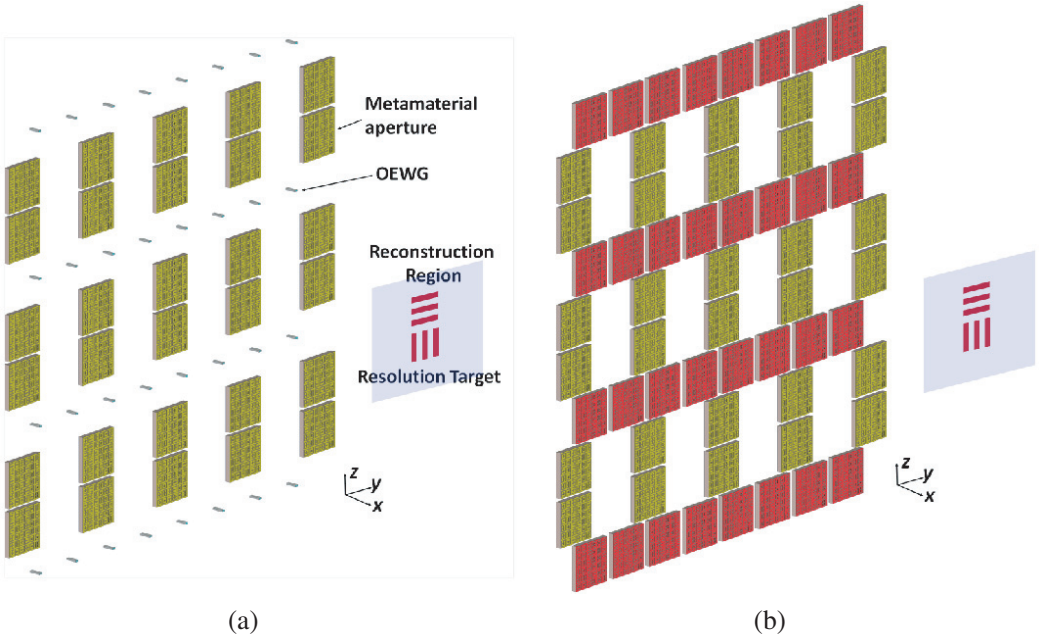

(a) (b)

Figure 1. Schematic of the multi-static imaging configuration consisting of (a) metamaterial apertures as transmitters and open ended waveguides and (b) metamaterial apertures as receivers respectively.

For the imaging scenario illustrated in Fig. 1, the frequency measurements collected by the receiving apertures are related to the scene reflectivity through the system transfer function or measurement matrix. Because the system is both diffraction and bandwidth limited, the problem can be reduced into a finite dimensional matrix equation [9, 11, 26],

$$\mathbf{g} = \mathbf{H}\ \mathbf{f} + n \tag{1}$$

where $\mathbf{g}$ is the measurement vector of dimension M (measurement number), $\mathbf{f}$ the scene reflectivity vector of dimension N (voxel number), $\mathbf{H}$ the measurement matrix of dimensions $M \times N$ whose rows and columns corresponds different measurement and scene locations, and n a noise term. As noted in the introduction, $\mathbf{H}$ corresponds to the system transfer function that relates the measured fields to the scene reflectivity distribution. Assuming the first Born approximation is sufficient to describe the field scattered from objects in the scene, the calculation of the $\mathbf{H}$ matrix can be simplified to [10, 11],

$$\mathbf{H}\left(\omega, \mathbf{r}_j\right) = \mathbf{E}^t\left(\omega, \mathbf{r}_j\right) \mathbf{E}^r\left(\omega, \mathbf{r}_j\right) \tag{2}$$

where $\mathbf{E}^t(\omega, \mathbf{r}_j)$ and $\mathbf{E}^r(\omega, \mathbf{r}_j)$ are the electric field waveforms at the scene location $\mathbf{r}_j$ generated by the transmitting and receiving apertures, respectively. For the simulations presented here, we do not

consider the details of a feed network, and assume the field measurement point and phase reference coincide with the feed point where the microwave energy is injected.

In general, Eq. (1) can be solved to estimate the scene reflectivity using a variety of numerical techniques [27]. For frequency diverse apertures considered here, the number of available measurements are limited by the number of panels, the system bandwidth, the aperture dimension, and the quality ($Q-$) factor associated with the metamaterial resonators [8–12]. For typically available Q-factors, the number of measurements (M) will fall short of the number of voxels needed for reconstruction (N), so that the scene can be significantly undersampled ($M \times N$). Furthermore the modes (measurements) in the frequency diverse imaging systems are highly correlated (the effective number of modes is less than the available number of measurements) thus making the system even more ill-conditioned unlike any SAR-like imaging systems. In such cases, the scene can be estimated through computational tools such as least square solvers [27] or compressive sensing algorithms such as TWIST (if the scene is suitably sparse) [28]. Compressive techniques in particular have been successfully implemented previously [8–12] to achieve high quality images; however, for the present study, these techniques may obscure the results by making assumptions about the scene. In fact, it was shown that compressive sensing techniques can be used for the compensation of phase errors [18–20]. Instead, here we use the well-known matched filter approach to estimate the scene, which can be expressed as

$$\mathbf{f}_{est} = \mathbf{H}^{*}\mathbf{g} \tag{3}$$

where $\mathbf{H}^{*}$ is the complex conjugate of measurement matrix, $\mathbf{H}$. Matched filter makes no assumption about the scene under test other than that the noise is white Gaussian in nature. This is due to the fact that the realistic system does not use active devices and previous experiments have also indicated that White Gaussian Noise is the primary source of noise [29]. Because the main purpose of this paper is to investigate the misalignment errors alone, we intentionally designed an oversampled system in order achieve high fidelity images, so we can isolate the effect of misalignment on the performance.

The fidelity of the reconstructed image heavily relies on the accuracy of the measurement matrix, $\mathbf{H}$. In an experiment, the only quantity that is measured is $\mathbf{g}$ and the scene is estimated using Eq. (3), where $\mathbf{H}$ is calculated using the knowledge of transmitter and receiver positions. In an ideal scenario and without any alignment errors, the measurement matrix, $\mathbf{H}$ in Eqs. (3) and (1), is constructed using the same assumptions regarding the aperture location and orientation. In practice, however, this perfect alignment is not the case due to some degree of characterization error resulting from misalignment. Any discrepancy in the location of a transmitter or receiver will translate primarily to a phase error in the measurement matrix (see Eq. (3)). It is important to note that although the apertures do not transmit at the same time, the information collected by the probes are processed coherently in Eq. (3) and thus the relative location and orientation of the transmitters and receivers are of utmost importance for the fidelity of the imaging process. Depending on the nature of misalignment (displacement or rotation), size and number of the apertures, the resulting phase error in the measurement matrix changes. Our goal in the following sections is to study each scenario and assess its effect on the overall performance of the system. Note that the results of this analysis will be dependent on specific system parameters. However, it obtains insight into effect of misalignments and provide with guidelines to minimize them while developing frequency-diverse imaging systems.

We consider metamaterial apertures that consist of a parallel plate waveguide with the top plate patterned with cELC irises as depicted in Fig. 2(b). The apertures are fed by a single coax from the center of the aperture. The frequency of operation is selected to be in the K-band (18–26.5 GHz), consistent with previous implementations [8–12]. The quality ($Q-$) factor of the metamaterial resonators is assumed to be $Q = 100$. The scene is sampled with 100 frequency sampling. As a result the total number of measurement is 72000 for the configuration considered here. The size of the metamaterial apertures is assumed to be 10 cm by 10 cm and the OEWG probes are modeled after standard WR42 (10.668×4.318) mm waveguide. The cELC elements are distributed randomly based on their resonant frequency on a regular grid with 5 mm separation. The total cELC radiator on a single panel is 400. The metamaterial transmitting apertures are arranged in pairs on a 5×3 grid as shown in Fig. 1 with spacing of 22 cm and 33 cm along y and z directions, respectively. The separation between each pair is 1 cm. The overall system size for the transmitting apertures is 97 cm by 87 cm. The receiving OEWG probes or metamaterial apertures are placed on a 8×4 regular grid with a separation of 16 cm in the y direction and 24 cm in the z direction, as shown in Figs. 1(a), (b) respectively. The overall receiving

aperture size for the OEWGs is 77 cm by 97 cm and for the metamaterial apertures is 87 cm by 107 cm. The origin is taken as the center of the configuration.

The imaging system of Fig. 1 consists of an electrically large metamaterial aperture illuminating a large region of interest in its Fresnel region. As a result, neither full-wave simulations nor analytical formulas are feasible options to perform end-to-end modeling of the system. Instead, we make use of a customized software that we refer to as the Virtualizer platform, developed in [9, 11]. This numerical tool provides scattering models for the frequency-diverse aperture as well as for the object being imaged, allowing for rapid simulation of imaging scenarios. While the Virtualizer tool makes approximations to enable fast computation, it provides a predictive model that captures the salient details of the imaging process [11]. The detailed discussion of this tool and the above formulation can be found in [9, 11].

3. RESULTS AND DISCUSSIONS

We divide our studies into two parts. First, we examine the effect of the displacement of the receiving apertures and OEWGs from their supposed locations. Next, we investigate how the rotation of apertures can affect the reconstructed images. We also examine how the misalignment sensitivity of the system changes as the system scales up and/or down in terms of the overall aperture size or number of feeds.

3.1. Displacement

To examine how the displacement of the apertures or OEWGs from their assumed locations impacts imaging performance, we simulate the system shown in Figs. 1(a), (b) for two cases, 1) OEWGs (Fig. 1(a)) used as receivers and 2) metamaterial sub-apertures (Fig. 2(b)) used as receiving antennas. In both studies, we keep the transmitting aperture positions unchanged and alter the positions of receivers only. In this manner, we can distinguish the effect of using metamaterial apertures as receivers compare to the OEWGs on the sensitivity to misalignment.

To emulate the effect of misalignment on the imaging process described in Eqs. (1) and (3), we first calculate the received signal, $\mathbf{g}$, using the default positions of the transmitting and receiving apertures. Next, the measurement matrix $\mathbf{H}$ in Eq. (3) is calculated assuming the receiving aperture positions have

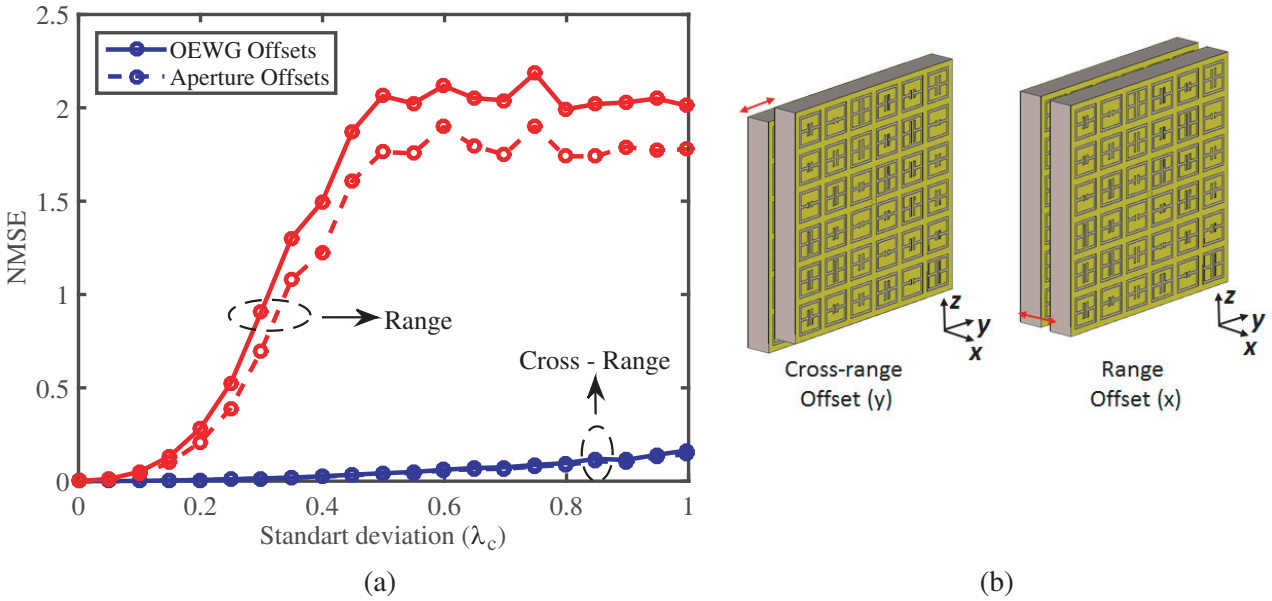

Figure 2. Normalized mean squared error (NMSE) of the reconstructed images as a function of displacement of OEWGs (solid line) and apertures (dashed-line) along cross-range (blue line) and range (red line) directions. The standard deviation is reported in terms of the center wavelength of frequency range ($\lambda_c = 1.36$) cm. (b) The depiction of aperture displacements in cross-range and range direction.

been displaced randomly. To keep our analysis close to a practical implementation, the displacement is drawn from a normal distribution with zero mean and different standard deviations. The images obtained at various standard deviations are examined to assess the sensitivity of our system to such errors. In order to quantify this sensitivity, we use the normalized mean square error (NMSE) defined as:

$$\mathbf{NMSE} = \frac{\sum |\mathbf{f}_{est} - \mathbf{f}|^2}{\sum |\mathbf{f}|^2} \tag{4}$$

Here $\mathbf{f}$ represents the scene estimate for the ideal condition of the system where no alignment errors are included (not the true target). While knowledge of the NMSE may not directly represent the imaging performance, it provides a simple means of assessing the degradation of image quality from its ideal condition. For each standard deviation value, the simulation was performed 100 times and the average NMSE value was calculated.

We examine the reconstructed images of a resolution target located at a distance $x = 1\,\mathrm{m}$. This target, which is common in practice for examining imaging performance, is selected due to its complex yet distinct features which will allow us to track the errors caused by misalignment. It is important to note that throughout this paper, we focus on oversampled scenarios. This setting ensures that observed degradation of image is due to alignment errors rather than ill-conditioned imaging. The resolution target consists of three horizontal metallic bars and three vertical bars, all of which are separated by 2.5 cm as depicted in Fig. 1. It is well known that the resolution of the system can be found through point spread function (PSF). For the configuration considered here the cross-range resolution is 1.5 cm in y direction and 1.16 cm in z direction and the range resolution is 2 cm. The reconstruction area is selected to be 22.5 cm in the y direction and 37.5 cm in the z direction. The image is reconstructed over a 2 cm depth in the x direction with a reconstruction pixel size of 5 mm in every direction for smooth image reconstruction. For the given region of interest and resolution of the system the space bandwidth product (SBP) is calculated as 609 [24]. Here, we assume the system is noiseless to focus on the effects solely of displacement. The NMSE for various displacement values for both OEWGs (solid line) and apertures (dashed line) are shown in Fig. 2(a). We note that the system shows similar behavior to displacement errors, whether the apertures or OEWGs are used as receivers. Thus SAR-like systems (such as multi-static systems) with simple antennas will also be susceptible to such misalignment errors. Furthermore, it can be seen that the effect of displacement errors in the cross range (blue line) direction (y) is less substantial compared with errors in the range (red line) direction (x). This difference is due to the fact that displacement in cross range has only a small effect on the measured phase of the back-scattered signal for objects placed in boresight. However, any displacement in range (x axis) directly translates to phase error, thus profoundly degrading the image. Note that the measured phase error depends on the path length between the transmitter, object, and receiver.

Figure 3(a) shows sample reconstructed images with selected standard deviations for displacements. Specifically, Figs. 3(a), (b) show reconstructed images when OEWGs or metamaterial apertures are used as receiving apertures with different standard deviations of $0\lambda_c = 0\,\mathrm{mm}$, $0.25\lambda_c = 0.34\,\mathrm{cm}$, $0.5\lambda_c = 0.68\,\mathrm{cm}$ and $1\lambda_c = 1.36\,\mathrm{cm}$ along y (cross-range) axis. Fig. 3(c) shows the reconstructed images when metamaterial apertures are used as receiving apertures with displacement described by standard deviation of $0\lambda_c = 0\,\mathrm{mm}$, $0.1\lambda_c = 1.36\,\mathrm{mm}$, $0.2\lambda_c = 2.7\,\mathrm{mm}$, and $0.3\lambda_c = 4.1\,\mathrm{mm}$ along x (range) axis. Note that the image is altered very little when the locations of OEWGs (a) or metamaterial apertures (b) have a displacement error even on the order of λ_c (or 1.36 cm) in the cross-range (y) direction, whereas the image quickly deteriorates when the receiver apertures have a displacement error on the order of $0.2\lambda_c$ (or 2.7 mm) in the range (x) direction. The tolerable misalignment errors can be established by examining the results depicted in Figs. 2 and 3. Note that an acceptable error level can vary for a specific system configuration. For instance, if 0.25 NMSE error is considered as the maximum level of the tolerable error, more than $0.2\lambda_c$ displacement in the range (x) cannot be tolerated. This prediction is confirmed by the degraded image plotted in Fig. 3(c). In this case, $0.2\lambda_c$ error corresponds to 72° in maximum (when the target is boresight of the displaced aperture) phase error at the center frequency of operation. This phase error will be smaller when the displaced aperture is not at boresight. Thus the average phase error will be less for all of the displaced apertures are combined. Note also that the image quality is better when metamaterial apertures are used instead of OEGWs as receiving apertures [25].

The configuration depicted in Fig. 1 is an illustrative example of a metamaterial based frequency

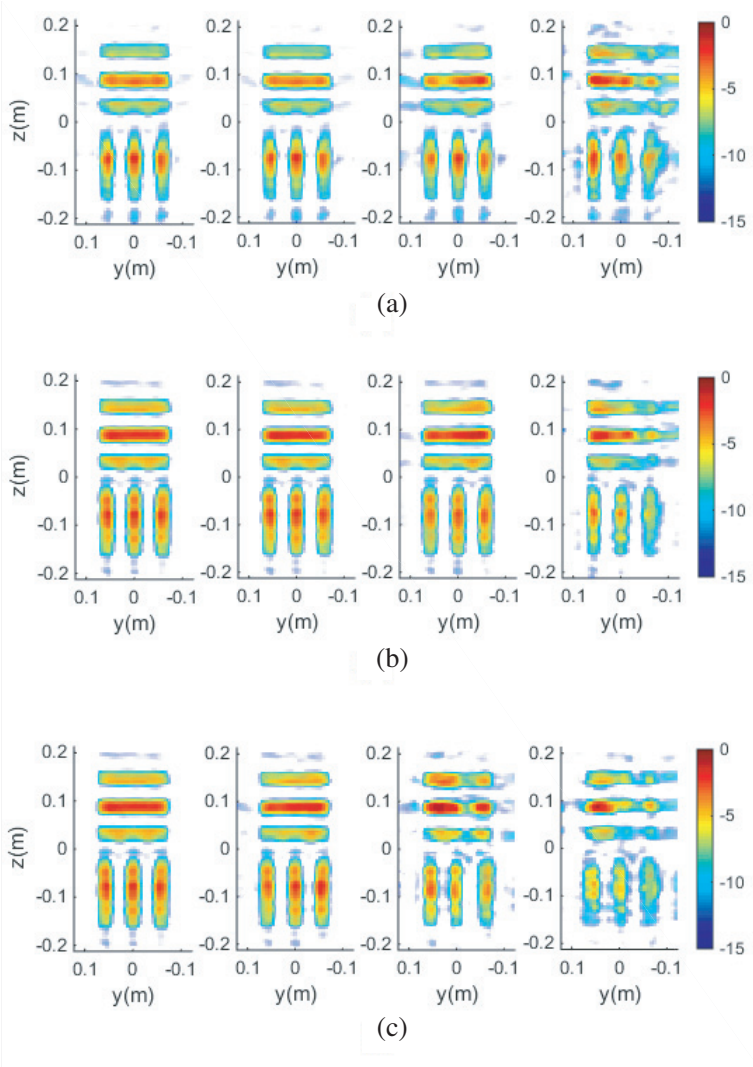

Figure 3. Examples of reconstructed images with different levels of misalignment for a particular random displacement. Plotted in (a) are images with alignment errors along y (cross-range) axis when using probes as receiving apertures. The standard deviation of the misalignment increases from left to right: $(0, 0.25\lambda_c, 0.5\lambda_c,$ and $\lambda_c)$ with associated NMSE values of (0, 0.0047, 0.04, and 0.232). Plotted in (b) are images with alignment errors along y (cross-range) axis when metamaterial apertures are used as receiving apertures. The standard deviation of the misalignment increases from left to right: $(0, 0.25\lambda_c, 0.5\lambda_c,$ and $\lambda_c)$ with NMSE of (0, 0.005, 0.034, and 0.187). Plotted in (c) are images with alignment errors along x (range) axis when metamaterial apertures are used as receiving apertures $(0, 0.1\lambda_c, 0.2\lambda_c,$ and $0.3\lambda_c)$ with NMSE of (0, 0.03, 0.23, and 0.36).

diverse imaging system. Depending on the application requirement, the overall system size can be smaller or larger in practice. Thus it is also important to examine how the sensitivity changes as the system size changes. Fig. 4 shows the result of this study when a different number of apertures are used with same configuration pattern. Three different configurations are studied. The transmitting apertures (as pairs) are placed on a grid of 4×2 (16 apertures), 5×3 (30 apertures), and 6×4 (48 apertures), respectively. Similarly the receiving apertures are placed on a grid of 6×3 (18 apertures), 8×4 (24 apertures), and 10×5 (50 apertures) as depicted in Fig. 4(b) respectively. Clearly, as the total number of apertures and the system size increases, the system sensitivity to displacement errors decreases. This is also consistent with previous results where the phase errors are decreased as the apertures are far from the boresight.

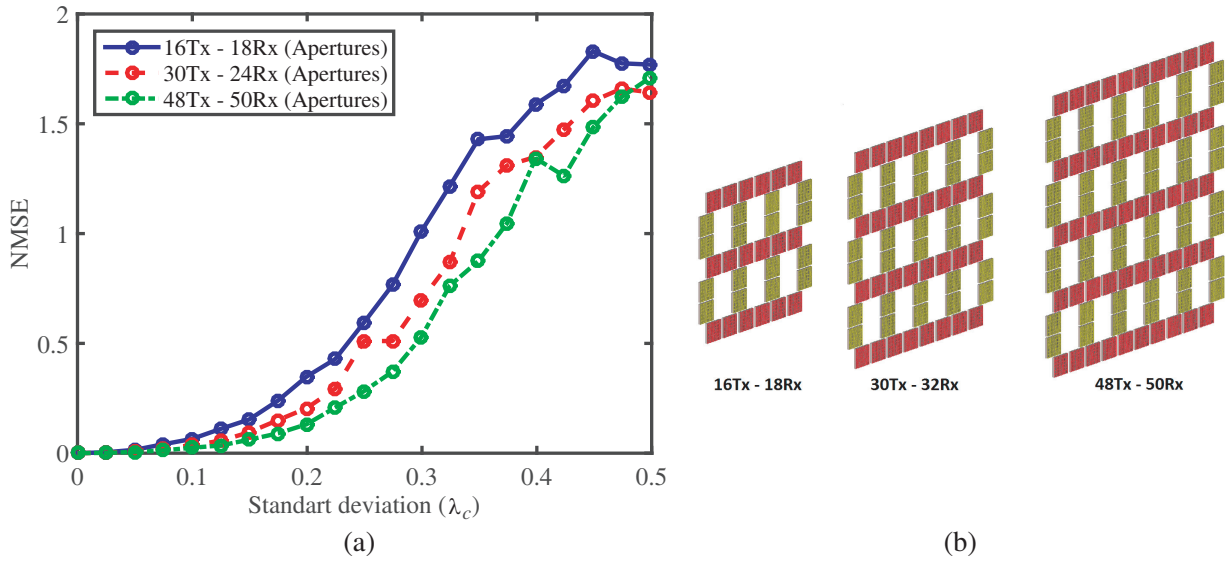

Figure 4. NMSE of the reconstructed images as a function of displacement error of receiving apertures along x axis as the number of aperture increases. (b) The scale up of the system.

3.2. Rotation

Another potential source of error in practice is rotation of the apertures from their assumed orientation. This problem can occur during both experimental characterization and installation of the sub-apertures on the composite system. Warping or bending of mounted apertures can also contribute to such problems. Again, in order to isolate the effect for metamaterial apertures and OEWGs, this time we keep the receiving sub-aperture and OEWG orientations unchanged and alter the orientations of the transmitting apertures only where we assume the error due to the rotation of OEWG is negligible. The transmitting aperture orientations are rotated around the three axes randomly using a normal probability distribution with zero mean for different standard deviations. The effect of rotational error (between 0 and 5 degrees) on the reconstructed images is shown in Fig. 5 for rotations around various axes (Fig. 5(b)). Clearly, the effect of rotational errors is very small (see error levels) compared with displacement errors in the range (x) direction, but comparable with the displacement errors in the cross-range (y) direction both when the sub-apertures or the OEWGs are used as receiving apertures. Interestingly the error is higher when OEWGs are used as receiving apertures. This can be explained by the fact that apertures do not have a well-defined phase center and thus the effective path between transmitters, target, and receiving aperture is averaged for the radiating elements of the aperture, reducing the phase error compared with that of the case when OEWGs are used as receivers. Also it can be noted that the error associated with rotations around the y or z axes is more prominent for apertures compared with rotations around the x axis. This is expected since rotations around the y or z axes can be approximated to first order as displacements along the x axis, thus, impacting the phase errors more drastically. It is also interesting to note that the effect of rotation around the y axis is more significant compared to the rotation around z axis. This is because the metamaterial elements and their effective magnetic moments, used in our analysis, are assumed to be oriented along the y direction. When excited by the cylindrical guided mode within the aperture, elements along the z axis get excited more strongly (the incident magnetic field is almost parallel to the metamaterial elements polarization).

The effect of rotational error on small (as compared to the sub-aperture sizes) antennas (OEWGs) is almost negligible compared with electrically-large sub-apertures (not shown here for brevity). Unlike conventional SAR systems that rely on mechanical scanning of simple antennas, the frequency-diverse system shown in Fig. 1 utilizes electrically-large metamaterial panels, and thus is more sensitive to rotational error. The degradation of the image due to rotational error becomes more prominent as the size of the apertures increases. This case is examined in Fig. 6 (configuration with OEWGs as receivers

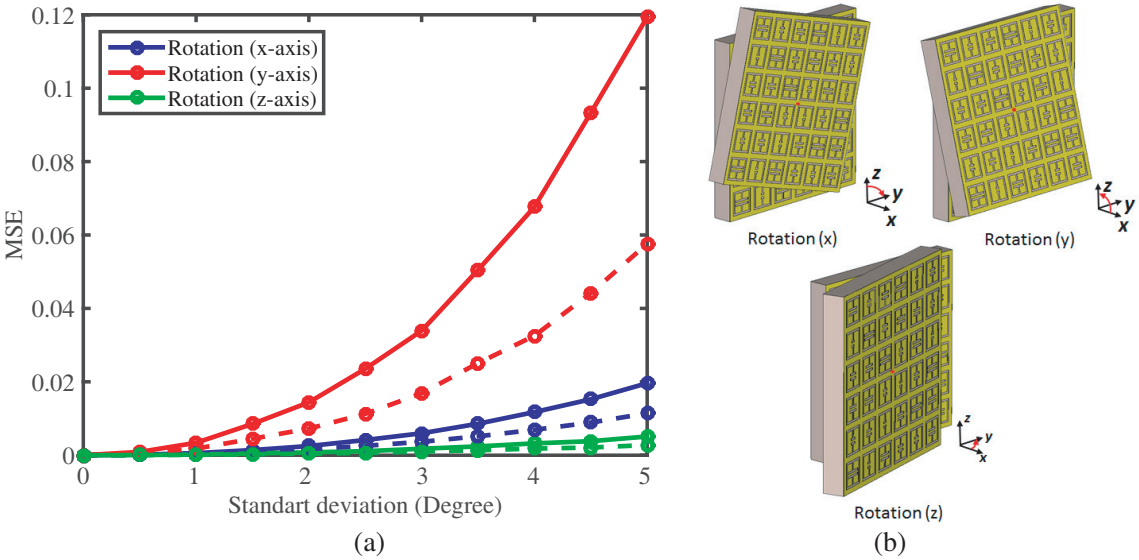

Figure 5. NMSE of the reconstructed images as a function of rotation of transmitting apertures around different axis when OEWGs (solid) or metamaterial apertures (dashed) are used as receiving apertures.

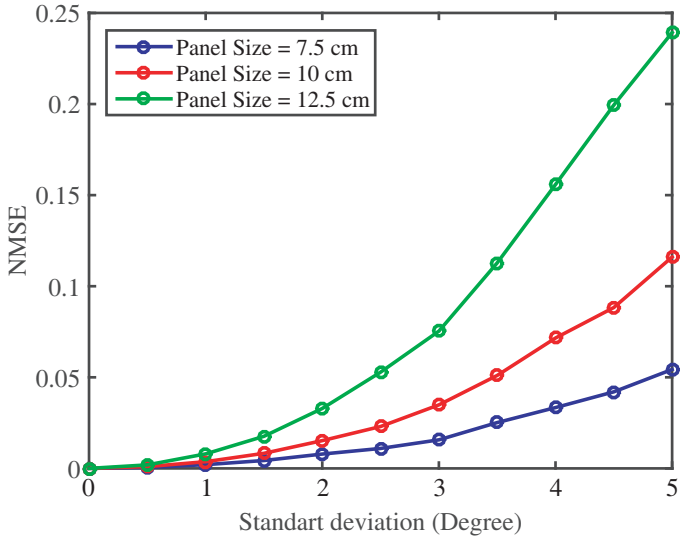

Figure 6. NMSE of the reconstructed images as a function of rotation error of transmitting apertures around y axis as the size of aperture increases. OEWGs are used as receiving apertures.

is used). The results are shown in Fig. 6 where the rotational error around the y axis is depicted for various sub-aperture (panel) sizes.

It should be noted that the total system size is changed accordingly for each aperture size. Clearly the error increases significantly even when the change of size is very small. This is expected because the error is dependent on the individual radiating elements on the apertures. Thus as the aperture size increases, the rotation causes more offset for those elements closer to edges. The results depicted in Fig. 6 suggest that using very large apertures may make the system extremely sensitive to rotational errors.

Another design parameter of relevance to metamaterial apertures is the number of feed points per panel. In the initial implementations, multiple feeds were employed for each electrically large aperture in order to excite the elements in the panel more efficiently [10, 12]. Using the same simulation approach, we

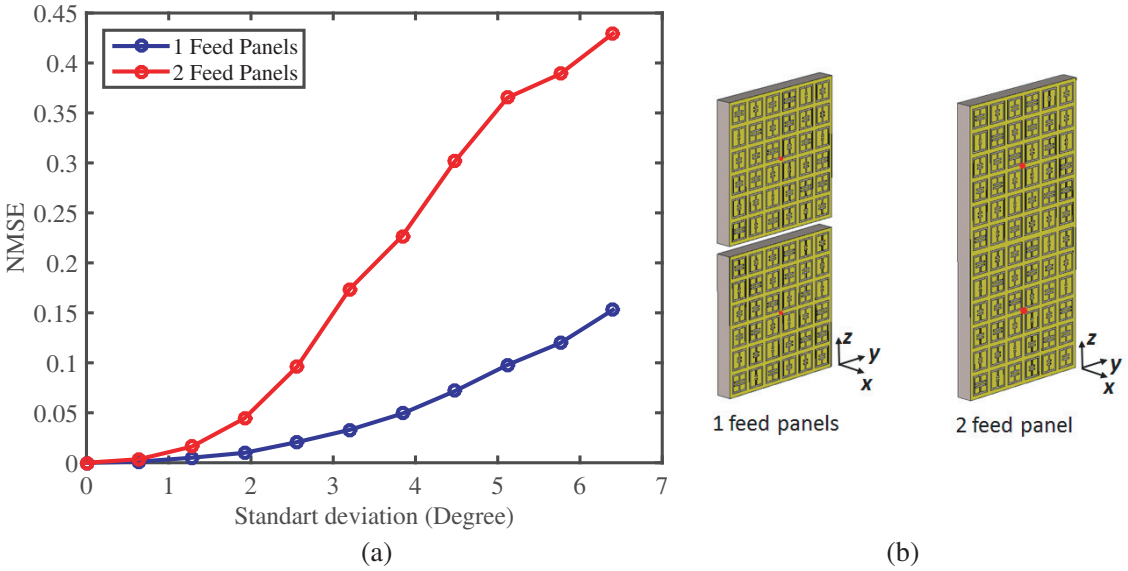

Figure 7. NMSE of the reconstructed images as a function of rotation error of transmitting apertures around y axis with single feed 10×10 cm and 2 feeds 10×20 cm panels respectively. OEWGs are used as receiving apertures. (b) 1 feed and 2 feed panels. Feed locations are indicated with red dot.

can examine the effect of the number of feeds per panel on the sensitivity of the system to misalignment. To be able to compare with the single feed apertures shown in Fig. 1, we consider apertures with two feeds where the adjacent transmitter apertures are combined into a single aperture with two feeds (see Fig. 7(b)). (In practice, the signal path of the two feeds are separated by a switch, keeping the number of measurement modes the same.) The result for this case is shown in Fig. 7(a). Not surprisingly, larger apertures with multiple feeds significantly amplifies the effect of rotational errors. Examining the results shown in Figs. 4 and 7, it is beneficial for to incorporate smaller apertures (each with a single feed) to manage and minimize the effect of rotational errors.

4. CONCLUSIONS

We have presented a systematic approach to investigating misalignment errors for frequency diverse imaging systems. Using this approach, we have analyzed the effects of misalignment errors for a multi-static imaging system based on frequency-diverse metamaterial apertures. We have shown that displacement errors, especially along the range direction, can significantly deteriorate the imaging capability of the system. This effect slowly decreases as the system size and the number of transmitters/receivers are increased. Unlike most conventional systems, frequency diverse imaging systems based on metamaterial apertures are also sensitive to rotational errors, since the system response relies on the individual metamaterial elements comprising the aperture. Because metamaterial apertures are electrically large, the rotational errors can offset the individual metamaterial elements significantly and result in a corruption of the phase information of the back-scattered signal. We have further shown that the rotational errors are pronounced when larger apertures and/or multiple feeds are used. While the studies conducted in this paper guides the design process of frequency-diverse apertures toward single-feed small panels, practical misalignment is still unavoidable. As a result, various additional measures should be taken to minimize such problems. For example, optical alignment fiducials can be integrated into the fabricated panels to allow for obtaining their precise location and orientation in aggregate system through optical cameras. Another important practical consideration is the alignment of the near-field scan stage with the fabricated panels under test. This can be done either through painstaking optical alignment of the stage or integration of RF fiducials in the aperture. These crucial practical examinations are the subject of our future work.

ACKNOWLEDGMENT

This work was supported by the Department of Homeland Security, Science & Technology Directorate (Contract No. HSHQDC-12-C-00049). The published material represents the position of the authors(s) and not necessarily that of the DHS.

REFERENCES

1. Sheen, D. M., D. L. McMakin, and T. E. Hall, "Three-dimensional milimeter-wave imaging for concealed weapon detection," *IEEE Transactions on Microwave Theory and Techniques*, Vol. 49, No. 9, 1581–1592, 2001.
2. Nikolova, N. K., "Microwave imaging for breast cancer," *IEEE Microwave Magazine*, Vol. 12, Issue 7, 78–94, 2011.
3. Wang, Y., and A. E. Fathy, "Advanced system level simulation platform for three-dimensional UWB through-wall imaging SAR using time-domain approach," *IEEE Transactions on Geoscience and Remote Sensing*, Vol. 50, No. 5, 1986–2000, 2012.
4. Chan, W. L., K. Charan, T. Dharmpal, K. F. Kelly, R. G. Baraniuk, and D. M. Mittleman, "A single-pixel terahertz imaging system based on compressed sensing," *Applied Physics Letters*, Vol. 93, No. 12, 121105, 2008.
5. Levy, U., H. C. Kim, C. H. Tsai, and Y. Fainman, "Near-IR demonstration of computer-generated holograms implemented using subwavelength gratings with space-variant orientation," *Opt. Letters*, Vol. 30, 2089–2091, 2005.
6. Watts, C. M., D. Shrekenhamer, J. Montoya, G. Lipworth, J. Hunt, T. Sleasman, S. Krishna, D. R. Smith, and W. J. Padilla, "Terahertz compressive imaging with metamaterial spatial light modulators," *Nature Photonics*, Vol. 8, Issue 8, 605–609, 2014.
7. Liutkus, A., D. Martina, S. Popoff, G. Chardon, O. Katz, G. Lerosey, S. Gigan, L. Daudet, and I. Carron, "Imaging with nature: Compressive imaging using a multiply scattering medium," *Scientific Reports*, Vol. 4, 5552, 2014.
8. Hunt, J., T. Driscoll, A. Mrozack, G. Lipworth, M. Reynolds, D. Brady, and D. R. Smith, "Metamaterial apertures for computational imaging," *Science*, Vol. 339, No. 6117, 310–313, 2013.
9. Lipworth, G., A. Mrozack, J. Hunt, D. L. Marks, T. Driscoll, D. Brady, and D. R. Smith, "Metamaterial apertures for coherent computational imaging on the physical layer," *Journal of the Optical Society of America A*, Vol. 30, Issue 8, 1603–1612, 2013.
10. Hunt, J., J. Gollub, T. Driscoll, G. Lipworth, A. Mrozack, M. Reynolds, D. J. Brady, and D. R. Smith, "Metamaterial microwave holographic imaging system," *Journal of the Optical Society of America A*, Vol. 31, Issue 10, 2109–2119, 2014.
11. Lipworth, G., A. Rose, O. Yurduseven, V. R. Gowda, M. F. Imani, H. Odabasi, P. Trofatter, J. Gollub, and D. R. Smith, "Comprehensive simulation platform for a metamaterial imaging system," *Appl. Opt.*, Vol. 54, Issue 31, 9343–9353, 2015.
12. Yurduseven, O., M. F. Imani, H. Odabasi, J. Gollub, G. Lipworth, A. Rose, and D. R. Smith, "Resolution of the frequency diverse metamaterial aperture imager," *Progress In Electromagnetics Research*, Vol. 150, 97–107, 2015.
13. Hand, T. H., J. Gollub, S. Sajuyigbe, D. R. Smith, and S. A. Cummer, "Characterization of complementary electric field coupled resonant surfaces," *Appl. Phys. Lett.*, Vol. 93, 212504, 2008.
14. Wahl, D. E., P. H. Eichel, D. C. Ghiglia, and C. V. Jakowatz, "Phase gradient autofocus-a robust tool for high resolution SAR phase correction," *IEEE Transactions on Aerospace and Electronic Systems*, Vol. 30, Issue 3, 827–835, 1994.
15. Ye, W., T. S. Yeo, and Z. Bao, "Weighted least-squares estimation of phase errors for SAR/ISAR autofocus," *IEEE Transactions on Geoscience and Remote Sensing*, Vol. 37, Issue 5, 2487–2892, 1999.
16. Li, X., G. Liu, and J. Ni, "Autofocusing of ISAR images based on entropy minimization," *IEEE Transactions on Aerospace and Electronic Systems*, Vol. 35, Issue 4, 1240–1252, 1999.

17. Li, J., R. Wu, and V. C. Chen, "Robust autofocus algorithm for ISAR imaging of moving targets," *IEEE Transactions on Aerospace and Electronic Systems*, Vol. 37, Issue 3, 1056–1069, 2001.
18. Blacknell, D., A. Freeman, S. Quegan, and I. A. Ward, "Geometric accuracy in airborne SAR images," *IEEE Transactions on Aerospace and Electronic Systems*, Vol. 25, Issue 2, 241–258, 1989.
19. Fornaro, G., G. Franceschetti, and S. Perna, "Motion compensation errors: Effects on the accuracy of airborne SAR images," *IEEE Transactions on Aerospace and Electronic Systems*, Vol. 41, Issue 4, 1338–1352, 2005.
20. Alvarez, Y., Y. Rodriguez-Vaqueiro, B. Gonzalez-Valdez, and J. A. Martinez-Lorenzo, "Phase error compensation in imaging systems using compressed sensing techniques," *IEEE Antennas and Wireless Propagation Letters*, Vol. 12, 1574–1577, 2013.
21. Ugur, S. and O. Arikan, "SAR image reconstruction and autofocus by compressed sensing," *Digital Signal Processing*, Vol. 22, Issue 6, 923–932, 2012.
22. Tian, J., J. Sun, X. Han, and B. Zhang, "Motion compensation for compressive sensing SAR imaging with autofocus," *2011 6th IEEE Conference on Industrial Electronics and Applications*, 1564–1567, 2011.
23. Fromenteze, T., O. Yurduseven, M. F. Imani, J. Gollub, C. Decroze, D. Carsenat, and S. Perna, "Computational imaging using a mode-mixing cavity at microwave frequencies," *Appl. Phys. Lett.*, Vol. 106, 194104, 2015.
24. Sleasman, T., M. F. Imani, J. N. Gollub, and D. S. Smith, "Dynamic metamaterial aperture for microwave imaging," *Appl. Phys. Lett.*, Vol. 107, 204104, 2015.
25. Marks, D. L., J. Gollub, and D. R. Smith, "Spatially resolving antenna arrays using frequency diversity," *Journal of the Optical Society of America A*, Vol. 33, Issue 5, 899–912, 2016.
26. Brady, D. J., *Optical Imaging and Spectroscopy*, Wiley and OSA, 2009.
27. Barrett, R., M. Berry, T. F. Chan, J. Demmel, J. Donato, J. Dongarra, V. Eijkhout, R. Pozo, C. Romine, and H. V. Der Vorst, *Templates for the Solution of Linear Systems: Building Blocks for Iterative Methods*, 2nd Edition, SIAM, Philadelphia, 1994.
28. Bioucas-Dias, J. M. and M. A. T. Figueiredo, "A new TwIST: Two-step iterative shrinkage/thresholding algorithms for image restoration," *IEEE Transactions on Image Processing*, Vol. 16, Issue 12, 2992–3004, 2007.
29. Hunt, J. D., *Metamaterials for Computational Imaging*, Duke University, 2013.